Shadow of rotating black hole surrounded by dark matter

Haiyuan Feng[a],[1,†] Ziqiang Cai,[2,‡] Rong-Jia Yang,[3,§] and Jinjun Zhang[e1,**]

[1] *School of Physics and Electronic Engineering, Shanxi Normal University, Taiyuan 030031, China*

[2] *College of Physics, Guizhou University, Guiyang 550025, China*

[3] *College of Physical Science and Technology, Hebei University, Baoding 071002, China*

arXiv:2604.11822v2 [gr-qc] 25 May 2026

Abstract

Dark matter (DM), a fundamental cosmic component, motivates the study of its influence on black hole (BH) shadows, especially for spinning BHs confirmed by EHT observations. This work generalizes the Schwarzschild BH surrounded by DM to an axisymmetric Kerr BH using the Newman–Janis Algorithm (NJA), investigating the resulting event horizon and ergosphere structures. Employing null geodesics, we examine the effects of DM mass (ΔM) on BH shadow, including its radius, distortion, and the associated energy emission rate. Our analysis reveals that DM has a negligible effect below a critical mass, once this threshold is surpassed, all BH structures expand significantly. Furthermore, DM robustly contributes to the shadow maintaining a near circular shape, even for highly spinning BHs. This pronounced structural expansion under high DM mass may potentially exceed current observational constraints, suggesting that DM must either be absent in the immediate vicinity of the BH or its localized mass must remain below this critical value to be consistent with astrophysical observations.

[a] Corresponding author

[e] Corresponding author

[†] Email address: fenghaiyuan@sxnu.edu.cn

[‡] Email address: gs.zqcai24@gzu.edu.cn

[§] Email address: yangrongjia@tsinghua.org.cn

[**] Email address: zhangjinjun@sxnu.edu.cn

I. INTRODUCTION

Einstein's general relativity (GR) fundamentally reshaped our view of spacetime and gravity, leading naturally to the prediction of black holes (BHs). Recent progress in gravitational experiments has ushered in a new stage in which electromagnetic observations can be used to probe the physical properties of ultra-compact objects such as BHs. Among the most significant achievements are the Event Horizon Telescope (EHT) measurements, which captured emission from the hot plasma circulating around the supermassive sources at the centers of M87 and the Milky Way [1–11], as well as infrared flare detections near the Galactic center by the gravity instrument [12, 13]. These developments provide an unprecedented opportunity to test BHs physics observationally, enabling detailed comparisons between high-resolution images and predictions obtained from General Relativistic Magneto-HydroDynamic (GRMHD) simulations of accreting plasma flows [14, 15].

It is remarkable that such high-precision observations now allow us to place stringent constraints on physically motivated BHs. In turn, this enables direct tests of GR and its possible extensions by searching for subtle departures from the Kerr geometry. The Kerr geometry represents the unique stationary and axisymmetric vacuum solution of Einstein field equations [16]. Current observational breakthroughs are broadly consistent with this Kerr paradigm, which predicts that gravitational collapse in realistic astrophysical environments produces a rotating, electrically neutral BH [17–20]. As a result, the Kerr solution serves as the standard reference against which BH observations are interpreted, and any alternative spacetime must account for potential deviations from this framework.

In realistic astrophysical settings, the Kerr BH is not an isolated object but is immersed in a field of photons with diverse trajectories. Depending on their initial conditions, these photons may be captured by the event horizon, scatter back to infinity, or become temporarily confined to unstable circular orbits. The latter trajectories define the photon sphere, whose geometry delineates the boundary of the BH shadow. For an observer at large distance, the shadow-namely, the apparent dark silhouette-arises from the characteristic deflection of light in the strong-field region surrounding the BHs [21]. A non-rotating BHs produces an exactly circular shadow, while rotation introduces a growing asymmetry in the silhouette, with the degree of distortion directly linked to the spin. The investigation of BH shadows began with Synge's seminal analysis in the 1960s, where he derived the shadow cast by a

spherically symmetric Schwarzschild BH [22]. Luminet later incorporated a surrounding accretion disk into this framework and provided a detailed computation of the resulting shadow size and appearance [23]. Subsequent extensions to rotating geometries demonstrated that the shadow of Kerr BH is no longer perfectly circular; instead, frame-dragging induces a characteristic asymmetry that encodes information about the spin [24]. These early developments laid the foundation for an extensive body of work exploring shadow structures in a wide variety of spacetime configurations. Recent studies have examined noncircular shadow features associated with alternative BH solutions [25–35] and horizonless compact objects such as wormholes [36–43], motivated by the possibility that shadow morphology may serve as a discriminating probe of gravitational dynamics beyond the standard Kerr paradigm.

Meanwhile, cosmological measurements indicate that nearly 85% of the matter content of the Universe is composed of nonluminous dark matter (DM) [44]. Observations of stellar rotation curves—particularly the unexpectedly large orbital velocities of stars in the outer regions of galaxies—demonstrate that the visible galactic disk resides within an extended, approximately spherical DM halo [45, 46]. This unseen component dominates the galactic mass budget and plays a central role in shaping the gravitational potential on both galactic and cosmological scales. Despite its overwhelming gravitational presence, the fundamental particle nature of DM remains fundamentally unknown. Numerous direct detection experiments most notably those targeting Weakly Interacting Massive Particles (WIMPs) have thus far yielded no conclusive evidence, challenging several of the leading particle physics candidates. While experiments such as the Cryogenic Dark Matter Search (CDMS) and DAMA/LIBRA have reported possible signals, these claims remain highly controversial, resulting in a mixed and often contradictory experimental landscape [47–52]. This persistent uncertainty further motivates astrophysical and gravitational probes, where the macroscopic effects of DM may offer complementary insights into its fundamental properties.

The advent of horizon scale BH imaging has opened a new avenue for investigating DM through its subtle imprints on BH observables. The presence of DM halo surrounding a compact object can modify the propagation of photons in its vicinity, leading to measurable departures in both the silhouette of the BH shadow and the weak gravitational deflection of light. In the context of EHT observations, such halos may enlarge the apparent shadow radius or introduce shape distortions that cannot be attributed solely to GR. Likewise, DM distributed near BHs can induce additional lensing effects, producing small but potentially

detectable deviations in the trajectories of photons from background sources [53–75]. These phenomena provide a complementary, indirect means of probing the properties of DM within strong gravity environments. In this paper, we extend the simplest DM model introduced in Ref. [28] to axisymmetric geometries by employing the Newman–Janis Algorithm (NJA). Within this framework, we aim to investigate the properties of the photon ring and the BH shadow, with particular emphasis on exploring how DM influences shadow related observables.

The parts of this paper are organized as follows. In Sec. II, we will introduce Schwarzschild BH surrounded by DM and investigate the influence of DM mass on the event horizon, photon sphere, and shadow radius. In Sec. III, we will extend the Schwarzschild BH surrounded by DM to the axisymmetric case and further analyzed the event horizon and ergosphere structures of BH. Furthermore, we will study the null geodesic equations of Kerr BH surrounded by DM and examined the resulting shadow properties. By tracing photon trajectories, we will derive explicit expressions for the two impact parameters and present the corresponding shadow images in celestial coordinates. In addition, we will analyze the dependence of the shadow radius, the distortion, and the BH energy emission rate on the DM mass. Finally, we summarize the main results and conclusions.

II. SCHWARZSCHILD BLACK HOLE SURROUNDED BY DARK MATTER

The unusually high orbital velocities of stars in the outer regions of galaxies suggest that the luminous disks of these galaxies are embedded within a significantly larger, roughly spherical halo composed of DM. This DM halo, which envelops the central BH, may induce minor deviations from the standard spacetime geometry near the BH horizon. Moreover, the characteristic shape of the shadow image is influenced by the local environment around the BH, whereas the contour of the shadow is determined solely by the spacetime metric itself. Along this line of reasoning, BH solutions incorporating a DM halo and their impact on the BH shadow have emerged as a prominent area of research in recent years [76–82]. A key question is how the distribution of DM modifies the spacetime surrounding the galactic center BH, and a crucial aspect of this problem involves solving the Einstein field equations in the presence of DM. Several efforts in this direction have been reported in Refs. [80–83]; a related investigation concerning dark energy was carried out in Ref. [84]. Nevertheless, in

all of these studies, some specific equation of state for DM or dark energy was presumed, rendering the outcomes highly dependent on the chosen model. Accordingly, we adopt the framework presented in Refs. [28, 85], which describes Schwarzschild BH embedded in a surrounding DM distribution.

The construction relies on two key assumptions. First, the DM is taken to be nonluminous and electromagnetically inert, allowing photons to traverse the medium without absorption. This assumption would break down for certain baryonic DM scenarios, where significant attenuation of light could occur and the interpretation would then depend on the detailed distribution and equation of state of the baryonic component. Second, the DM carries a finite mass density, which may be incorporated into the BH mass function as an effective additional mass. Although the model is fairly simplistic, it offers two advantages when describing the influence of DM on Schwarzschild BH. The model is characterized by independent fundamental parameters associated with the shell, namely the mass ratio $\Delta M/M$, the inner boundary position r_s, and the shell thickness Δr_s. Additionally, it can be applied to any type of DM—not only the component that binds the entire galaxy, but also locally confined variants, such as non-luminous stars (brown dwarfs), stellar-mass BHs, primordial BHs, non-radiating dust, and others—all of which are gravitationally captured by the central supermassive BH. Therefore, it is meaningful to discuss this model.

The Schwarzschild BH surrounded by DM can be written as [28]

$$ds^2 = -f(r)dt^2 + \frac{dr^2}{f(r)} + r^2\left(d\theta^2 + \sin^2\theta d\phi^2\right), \tag{1}$$

with

$$f(r) = 1 - \frac{m(r)}{r}, \tag{2}$$

where $m(r)$ denotes the mass function that incorporates the contribution from the surrounding DM. To account for the different physical regimes, the mass distribution is defined in a piecewise manner across three distinct radial domains, given by

$$m(r) = \begin{cases} M, & r < r_s \\ M + \Delta M\left(3 - 2\frac{r-r_s}{\Delta r_s}\right)\left(\frac{r-r_s}{\Delta r_s}\right)^2, & r_s \leq r \leq r_s + \Delta r_s \\ M + \Delta M, & r_s + \Delta r_s < r \end{cases} \tag{3}$$

where the functional $\left(3 - 2\frac{r-r_s}{\Delta r_s}\right)\left(\frac{r-r_s}{\Delta r_s}\right)^2$ is constructed to ensure the continuity of both $m(r)$ and its derivative $m'(r)$. As illustrated on the right panel of Fig. 1, the DM is

predominantly concentrated within the interval $r_s \leq r \leq r_s + \Delta r_s$. Using the Einstein field equations $G_{\mu\nu} = 8\pi T_{\mu\nu}$, one then obtain

$$T^t{}_t = T^r{}_r = -\frac{m'(r)}{4\pi r^2}, \tag{4}$$

and

$$T^\theta{}_\theta = T^\phi{}_\phi = -\frac{m''(r)}{8\pi r}. \tag{5}$$

It is evident that both the density and pressure depend solely on the first and second derivatives of the mass function. Since the chosen mass profile is smooth, these derivatives are well defined throughout the domain. We also remark that the DM surrounding the BH may, in principle, fall into two categories: a configuration with positive energy density ($\Delta M > 0$), corresponding to ordinary matter, and one with negative energy density ($\Delta M < 0$). We will restrict our analysis to the physically motivated case $\Delta M > 0$.

Additionally, the left panel of Fig. 1 shows the radial dependence of the metric function $f(r)$. We find that when the DM mass ΔM becomes sufficiently large, its gravitational effect can shift the location of the Schwarzschild event horizon, thereby modifying the underlying BH structure. The metric function possesses a critical point r_*, at which the presence of DM leads to the formation of a single horizon. Based on panels $f(r_*, \Delta M) = 0$ and $f'(r_*, \Delta M) = 0$, this critical value is determined to be $r_*/M = 152$ with the corresponding mass parameter $\Delta M/M = 800/9$. In other words, when $\Delta M/M < 800/9$, the DM does not affect the position of the event horizon.

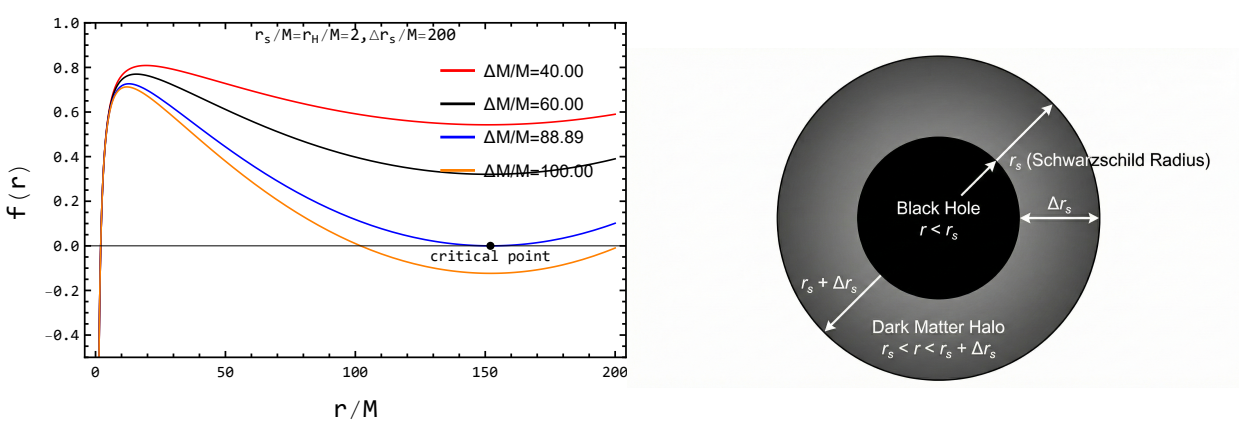

FIG. 1: The left panel shows the corresponding radial dependence of $f(r)$, while the right panel illustrates the radial distribution of DM surrounding the Schwarzschild BH. In these plots, we fix the parameters to $r_s/M = 2$ and $\Delta r_s/M = 200$.

A. Photon sphere radius and shadow structure of Schwarzschild black hole surrounded by dark matter

For a generic static and spherically symmetric spacetime, the location of the photon sphere can be determined following the procedure outlined in Refs. [28, 86–90]. In such geometries, null geodesics admit an effective potential whose extremum corresponds to unstable circular photon orbits. By imposing the condition that the radial derivative of the effective potential vanishes, one obtains the photon sphere radius, which satisfies

$$2f(r_{\rm ph}) = r_{\rm ph} f'(r_{\rm ph}). \tag{6}$$

This condition provides a general and coordinate independent criterion for identifying the photon sphere in any static, spherically symmetric metric. For the Schwarzschild BH surrounded by DM, as described by Eq. (1), previous studies have provided a detailed analysis of the associated photon sphere [28]. The main results relevant to our discussion can be summarized as follows.

1: The DM is distributed such that the photon sphere lies between the event horizon $r_{\rm H}/M = 2$ and the inner boundary of DM layer r_s. Under these conditions, photons propagate entirely through the vacuum Schwarzschild region, and the resulting shadow coincides with that of Schwarzschild BH. Accordingly, the photon sphere radius retains its standard value $r_{\rm ph} = 3M$.

2: Photon sphere located outside the DM shell $r_s + \Delta r_s < r_{\rm ph} < r_o$. In such case, the effective mass governing photon orbits is simply the sum of the BH mass and the DM contribution, yielding $r_{\rm ph} = 3\big(M + \Delta M\big)$.

3: Physically relevant configuration: photon sphere located within the DM layer. The only scenario of real interest arises when the innermost unstable photon orbit is embedded inside the DM distribution, such that $r_s < r_{\rm ph} < r_s + \Delta r_s$. Solving the photon sphere condition with the metric functions leads to the following expression for the radius of the photon sphere:

$$r_{\rm ph} = \frac{-\sqrt{F}\Delta {\rm r}_s + 6\Delta {\rm M} r_s\left(r_s + \Delta {\rm r}_s\right) + \Delta {\rm r}_s^3}{3\Delta {\rm M}\left(2r_s + \Delta {\rm r}_s\right)}, \tag{7}$$

with

$$F \equiv 12\Delta M r_s \Delta r_s\left(\Delta r_s - 3M\right) - 18M\Delta M\Delta r_s^2 + 3\Delta M r_s^2\left(4\Delta r_s + 3\Delta M\right) + \Delta r_s^4. \tag{8}$$

Table 1 and 2 illustrate how the photon sphere location evolve as DM mass increases. Table 1 corresponds to the regime in which the DM mass is insufficient to modify the event horizon. In this case, increasing the mass leads to a slight reduction in the photon sphere radius. Table 2 corresponds to the regime in which the event horizon is modified, where the photon sphere radius increases by a significant factor. Physically, this trend is expected: the presence of additional matter in the vicinity of Schwarzschild BH effectively augments the total gravitational mass, thereby enlarging the fundamental length scales of the system.

Subsequently, following the notation introduced in Refs. [86–90], we denote by r_o the radial position of the observer and by α the angle measured with respect to the radial direction. Under these definitions, we obtain

$$\cot\alpha = \frac{\sqrt{g_{rr}}}{\sqrt{g_{\varphi\varphi}}}\frac{dr}{d\phi}\bigg|_{r=r_o} = \frac{r}{\sqrt{f(r)}}\frac{dr}{d\phi}\bigg|_{r=r_o}, \tag{9}$$

which links the geometric properties of photon trajectories to the shadow measured by a distant observer. Here we have restricted the photon motion to the equatorial plane $\theta = \pi/2$. With this choice, and by invoking elementary plane geometry considerations, one readily obtains the angular radius of the BH shadow.

$$\sin^2(\alpha_{\rm sh}) = \frac{h(r_{\rm ph})^2}{h(r_o)^2}, \tag{10}$$

where $h(r)$ is well-defined, $h(r)^2 = r/\sqrt{f(r)}$. In the conventional limit where the observer is located at spatial infinity, $r_o \to \infty$. In this case, the shadow radius can be derived

$$R_{\rm sh} = r_o \sin\alpha_{\rm sh}, \tag{11}$$

which serves as the principal physical quantity. Following the argument presented in Ref. [28], one can make use of the standard property of spherical systems: only the matter enclosed within a given radius contributes to the gravitational force at that radius. Building on this idea, Ref. [28] proposes an approximate result

$$R_{\rm sh} = r_o \sin\alpha_{\rm sh} \approx 3\sqrt{3}\left(M + \Delta{\rm M} - \frac{\Delta{\rm M}\left(-2r_s + 2r_{\rm ph} + \Delta{\rm r}_s\right)\left(r_s - r_{\rm ph} + \Delta{\rm r}_s\right)^2}{\Delta{\rm r}_s^3}\right). \tag{12}$$

The essential point is that only the DM inside the photon sphere affects the shadow formation, while the exterior distribution can be neglected. From Tables 1 and 2, it is evident that the DM mass can indeed modify the BH shadow radius. In particular, once the mass exceeds the critical value, the shadow radius increases significantly, consistent with the strengthened gravitational field generated by the additional mass.

TABLE I: Table summarizes the dimensionless physical quantities for the BH. We fix the parameters to $r_s/M = 2$ and $\Delta r_s/M = 200$.

BH	$\Delta M/M = 20$	$\Delta M/M = 30$	$\Delta M/M = 40$	$\Delta M/M = 50$	$\Delta M/M = 60$	$\Delta M/M = 70$
$r_{\rm ph}/M$	2.99554	2.99332	2.99111	2.98891	2.98671	2.98452
$R_{\rm sh}/M$	5.20392	5.20780	5.21169	5.21557	5.21946	5.22334

TABLE II: We present the variations of the relevant physical quantities in the regime where the DM mass is sufficiently large to modify the BH event horizon.

BH	$\Delta M/M = 100$	$\Delta M/M = 120$	$\Delta M/M = 140$	$\Delta M/M = 160$	$\Delta M/M = 180$	$\Delta M/M = 200$
$r_{\rm H}/M$	202	242	282	322	362	402
$r_{\rm ph}/M$	303	363	423	483	543	603
$R_{\rm sh}/M$	524.811	628.734	732.657	836.581	940.504	1044.430

III. ROTATING KERR BLACK HOLE SURROUNDED BY DARK MATTER

Considering rotating BHs is essential because astrophysical observations strongly suggest that most supermassive BHs possess significant angular momentum. Evidence from accretion disk spectroscopy, relativistic jet formation, and stellar orbital dynamics consistently indicates the presence of substantial spin, implying that a static BH description is insufficient. Moreover, the EHT images of M87* and Sgr A* reveal asymmetries in brightness and shadow structure that arise naturally from frame-dragging and other rotation-induced effects. Therefore, incorporating rotation is necessary for producing realistic photon trajectories and for achieving accurate comparisons between theoretical shadow predictions and observational data.

The Newman–Janis Algorithm (NJA) is a well-established procedure for generating rotating BH solutions from static metrics within the framework of GR [91, 92]. By employing a complex coordinate transformation together with a suitable tetrad representation, the NJA effectively introduces angular momentum into a non-rotating BH. This method has been widely used to construct rotating counterparts of various static solutions and provides a practical and physically motivated approach for exploring the geometry and observational

signatures of spinning BHs [93–97].

Following the conventional procedure, the first step is to rewrite the metric from Boyer–Lindquist (BL) coordinates into the Eddington–Finkelstein (EF) coordinates. This is achieved by applying an appropriate coordinate redefinition, which relates the time coordinate in BL form to the null coordinate u in EF form. Through this transformation, one obtains the EF coordinates required for implementing the subsequent steps of the NJA.

$$dt = du + \frac{dr}{f(r)}. \tag{13}$$

The metric then takes the following form

$$ds^2 = -f(r)du^2 - 2dudr + r^2 d\theta^2 + r^2 \sin^2\theta d\phi^2. \tag{14}$$

Using a null tetrad basis satisfying $l^\mu l_\mu = n^\mu n_\mu = m^\mu m_\mu = l^\mu m_\mu = n^\mu m_\mu = 0$ and $l^\mu n_\mu = -1, m^\mu \bar{m}_\mu = 1$, the corresponding contravariant metric can be written as

$$g^{\mu\nu} = -l^\mu n^\nu - l^\nu n^\mu + m^\mu \bar{m}^\nu + m^\nu \bar{m}^\mu, \tag{15}$$

with

$$\begin{aligned} l^\mu &= \delta^\mu_r, \\ n^\mu &= \delta^\mu_u - \frac{f(r)}{2}\delta^\mu_r, \\ m^\mu &= \frac{1}{\sqrt{2}r}\left(\delta^\mu_\theta + \frac{i}{\sin\theta}\delta^\mu_\phi\right), \\ \bar{m}^\mu &= \frac{1}{\sqrt{2}r}\left(\delta^\mu_\theta - \frac{i}{\sin\theta}\delta^\mu_\phi\right). \end{aligned} \tag{16}$$

Subsequently, we carry out the nontrivial coordinate transformations in the (u, r) plane

$$\begin{aligned} u &\to u - ia\cos\theta, \\ r &\to r + ia\cos\theta, \end{aligned} \tag{17}$$

where a is the spin parameter. Meanwhile, we postulate that these coordinate transformations deform the original metric functions into new angular and spin dependent structures, namely $f(r) \to F(r, a, \theta)$ and $r^2 \to \Sigma(r, a, \theta) = r^2 + a^2\cos^2\theta$ ($\lim_{a\to 0} F(r, a, \theta) = f(r), \lim_{a\to 0}\Sigma(r, a, \theta) = r^2$) [98, 99]. Under the same procedure, the null tetrads are likewise promoted to their transformed counterparts.

$$
\begin{aligned}
l^{\mu} &= \delta^{\mu}_{r}, \\
n^{\mu} &= \delta^{\mu}_{u} - \frac{F}{2}\delta^{\mu}_{r}, \\
m^{\mu} &= \frac{1}{\sqrt{2\Sigma}}\left(\left(\delta^{\mu}_{u} - \delta^{\mu}_{r}\right) ia\sin\theta + \delta^{\mu}_{\theta} + \frac{i}{\sin\theta}\delta^{\mu}_{\phi} \right), \\
\bar{m}^{\mu} &= \frac{1}{\sqrt{2\Sigma}}\left(-\left(\delta^{\mu}_{u} - \delta^{\mu}_{r}\right) ia\sin\theta + \delta^{\mu}_{\theta} - \frac{i}{\sin\theta}\delta^{\mu}_{\phi} \right).
\end{aligned}
\tag{18}
$$

Furthermore, the rotating metric in the EF coordinates is

$$
\begin{aligned}
\mathrm{d}s^2 = &- F\ \mathrm{d}u^2 - 2\ \mathrm{d}u\ \mathrm{d}r + 2a\left(F-1\right)\sin^2\theta\ \mathrm{d}u\ \mathrm{d}\phi + \Sigma \mathrm{d}\theta^2 \\
&+ 2a\sin^2\theta\ \mathrm{d}r\ \mathrm{d}\phi + \sin^2\theta\left[\Sigma + a^2\left(2-F\right)\sin^2\theta\right]\mathrm{d}\phi^2.
\end{aligned}
\tag{19}
$$

The final stage of the NJA involves restoring the metric in Eq. (19) to BL form. This is accomplished by applying the following coordinate redefinitions, which eliminate the mixed terms and yield the standard BL structure.

$$
\mathrm{d}u = \mathrm{d}t + \lambda(r)\mathrm{d}r, \qquad \mathrm{d}\phi = \mathrm{d}\phi' + \chi(r)\mathrm{d}r,
\tag{20}
$$

with

$$
\begin{aligned}
\lambda(r) &= -\frac{r^2 + a^2}{r^2 f(r) + a^2}, \\
\chi(r) &= -\frac{a}{r^2 f(r) + a^2}.
\end{aligned}
\tag{21}
$$

Subsequently we obtain

$$
F(r,a,\theta) = \frac{r^2 f(r) + a^2\cos^2\theta}{\Sigma}.
\tag{22}
$$

Then, the rotating extension of the Schwarzschild BH metric in the presence of DM can be expressed as

$$
\begin{aligned}
ds^2 = &-\left(1 - \frac{2\mathrm{Y}r}{\Sigma}\right)dt^2 + \frac{\Sigma}{\Delta}dr^2 + \Sigma d\theta^2 - \frac{4ar\sin^2\theta\mathrm{Y}}{\Sigma}dtd\phi \\
&+ \sin^2\theta\left[\frac{\left(r^2+a^2\right)^2 - a^2\Delta\sin^2\theta}{\Sigma}\right]d\phi^2
\end{aligned}
\tag{23}
$$

with

$$
\begin{aligned}
&\Delta(r,a) = r^2 f(r) + a^2 = r^2 - 2rm(r) + a^2, \\
&\mathrm{Y}(r) = \frac{r(1-f(r))}{2} = m(r), \\
&\Sigma(r,a,\theta) = r^2 + a^2\cos^2\theta,
\end{aligned}
\tag{24}
$$

where $f(r)$ is specified by Eq. (2), and a denotes the BH spin parameter. It is worth noting that we have reinstated $\phi' \to \phi$. We observe that the solution reduces to the Kerr BH in the limit $\Delta M = 0$. Furthermore, when the spin parameter is set to $a = 0$, the spacetime smoothly recovers the spherically symmetric configuration described by Eq. (1). Moreover, any rotating solution generated through this procedure must be checked against the Einstein field equations. Fortunately, based on Ref. [100], we have already demonstrated in Appendix A that this class of metrics indeed satisfies the field equations, and the corresponding DM density and pressure profiles have been provided by

$$\begin{aligned} \rho = -p_r &= \frac{\mathrm{m}'(r) r^2}{4\pi\Sigma^2}, \\ p_\theta = p_\phi = p_r &- \frac{\mathrm{m}''(r) r + 2\mathrm{m}'(r)}{8\pi\Sigma}. \end{aligned} \tag{25}$$

With this assurance in place, we can now proceed to analyze the physical properties of rotating Kerr BH surrounded by DM.

A. Event horizons

Following the methodology used for the spherically symmetric case, we note that the horizon of an axisymmetric BH is likewise determined by $\Delta(r, a)$. However, because the mass function is defined piecewise in our model, we obtain the relation

$$\Delta(r,a) = \begin{cases} r^2 + a^2 - 2rM, & r < r_s \\ r^2 + a^2 - 2rM - 2r\Delta M \left(3 - 2\frac{r - r_s}{\Delta r_s}\right)\left(\frac{r - r_s}{\Delta r_s}\right)^2, & r_s \leq r \leq r_s + \Delta r_s \\ r^2 + a^2 - 2rM - 2r\Delta M. & r_s + \Delta r_s < r \end{cases} \tag{26}$$

The horizons are clearly governed by the spin parameter a as well as the DM mass parameters ΔM and Δr_s. A numerical examination of Eq. (26) shows that, for certain parameter choices, the equation admits two distinct solutions. These solutions correspond to the Cauchy horizon r_- (the smaller root) and the event horizon r_+ (the larger root).

Figure 2 illustrates the dependence of $\Delta(r)$ on the BH parameters. In the left panel, we analyze the effect of the spin a while assuming DM mass too small to alter the underlying horizon structure. In this regime, two distinct roots are obtained for $|a/M| < 1$, whereas in the extremal limit $|a/M| \to 1$ the Cauchy and event horizons coalesce into a single degenerate root, mirroring the well-known behavior of the Kerr solution.

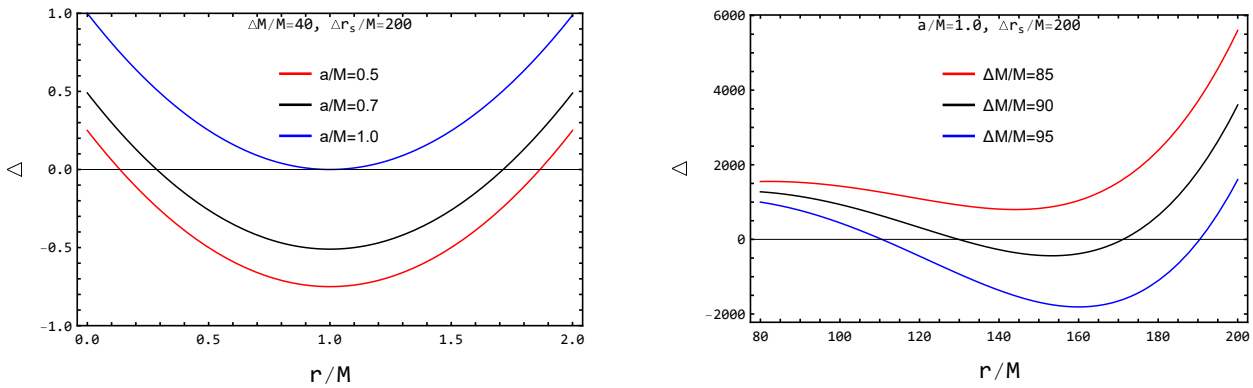

FIG. 2: The left panel illustrates the radial dependence of $\Delta(r)$, where the parameters $\Delta M/M = 40$ and $\Delta r_s/M = 200$ are held fixed. The red, black, and blue curves correspond to spin parameters $a = 0.5$, $a = 0.7$, and $a = 1.0$, respectively. In the right panel, we set $a = 1.0$ and $\Delta r_s/M = 200$ to examine whether the DM mass influences the horizon structure. The red, black, and blue curves represent $\Delta M/M = 85$, $\Delta M/M = 90$, and $\Delta M/M = 95$, respectively.

In contrast, the right panel of Fig. 2 examines the regime in which the DM mass becomes sufficiently large to modify the geometry. When the parameters a and Δr_s are fixed, the upper bound is determined by the conditions $\Delta(r_*) = 0$ and $\Delta'(r_*) = 0$. For the case $a/M = 1$ and $\Delta r_s/M = 200$, these equations yield $r_*/M = 150.5$ and $\Delta M/M = 88.3$. A critical upper limit for the DM mass emerges: the red curve, corresponding to a mass below this threshold, preserves the standard horizon configuration. However, the black and blue curves represent masses exceeding this limit, leading to a pronounced shift of the horizon radius, which increases by more than an order of magnitude. This substantial enlargement of the horizon closely parallels the trend identified in the spherically symmetric case.

B. Ergosphere

The ergosphere is defined as the region enclosed between the event horizon r_+ and the outer stationary limit surface. The stationary limit surface, also known as the infinite redshift surface, corresponds to the location where the metric component g_{tt} vanishes. Equivalently, it marks the boundary beyond which no observer can remain at rest relative to a distant inertial frame, due to the frame-dragging effect induced by the BH's rotation. The

inner and outer ergosurfaces are the two dimensional surfaces, which is

$$\begin{cases} r^2 + a^2\cos^2\theta - 2rM = 0, & r < r_s \\ r^2 + a^2\cos^2\theta - 2rM - 2r\Delta M\left(3 - 2\frac{r-r_s}{\Delta r_s}\right)\left(\frac{r-r_s}{\Delta r_s}\right)^2 = 0, & r_s \leq r \leq r_s + \Delta r_s \\ r^2 + a^2\cos^2\theta - 2rM - 2r\Delta M = 0. & r_s + \Delta r_s < r \end{cases} \tag{27}$$

The ergosphere structure is similarly composed of three distinct regions. By setting $r_s = r_+$ (The outer horizon of Kerr BH), only the latter two regions need to be considered, in line with the analysis of the horizon. When the DM mass is sufficiently large, it can shift the ergosphere's location. Figure 3 illustrates these effects. The first row shows the ergosphere for spin parameters $a/M = 0.5, 0.7, 1.0$, with $\Delta M/M = 40$, $\Delta r_s/M = 200$, and $\theta = \pi/4$ and 2π. Across different values of a, two distinct locations for the potential layers are observed. Only in the extremal case ($a/M = 1$) at $\theta = 2\pi$ does a single layer appear, which is consistent with the expected behavior of an extremal BH. The second row presents a particularly interesting scenario, in which the DM mass is sufficiently large to alter the ergosphere structure. We observe that for $\Delta M/M = 90$ (black curve) and $\Delta M/M = 95$ (blue curve), the contribution from the DM introduces additional roots in g_{tt}. In other words, the mass becomes large enough to significantly shift the location and shape of the ergosphere, demonstrating the strong influence of surrounding matter on the BH.

Figure 4 shows the horizon and ergosphere regions plotted in the (x, z) plane of Cartesian coordinate system centered on the BH. We take the largest and smallest roots as the outer and inner boundaries of horizon and ergosphere region, respectively. The two red curves denote the inner and outer boundaries of ergosphere, while the black curves represent inner and outer horizons. In the first row, we consider a relatively small DM mass, insufficient to modify the BH's structure, and examine the effect of varying the spin parameter a. As a approaches the extremal limit, the initially elliptical potential layers gradually separate into two nearly circular regions, while the horizons merge into a single surface. In the second row, larger DM masses generate new potential location and horizon regions, with the boundaries expanding substantially. In particular, in the last two panels, the red and black curves almost coincide, indicating that the geometric configuration has been completely altered. This behavior is physically consistent, as the increased DM mass enhances the gravitational field, thereby affecting the BH and modifying its spacetime structure.

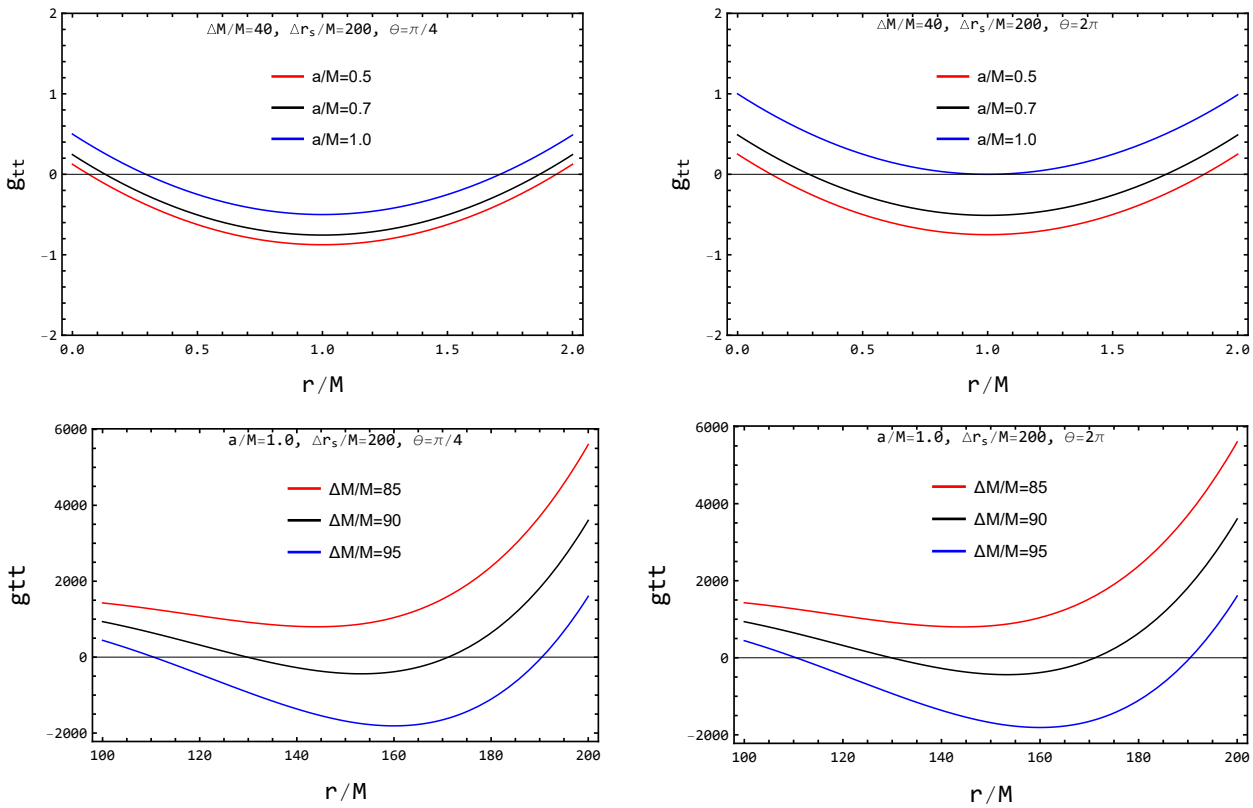

FIG. 3: The first row of the figure illustrates how the ergosphere varies with the spin parameter a. For each curve, the zeros of the function identify the locations of the two corresponding potential layers. The second row shows how the DM mass influences the locations of the ergosphere.

IV. NULL GEODESICS AND SHADOW CAST

One of the central objectives is to determine the shadow cast by the BH described by metric Eq. (23). In Sec. II, we examined the spherically symmetric configuration. In this section, we turn to the axisymmetric case. In contrast to the earlier results, the conclusions obtained here are expected to provide a more faithful representation of realistic astrophysical BH environments. To achieve this, we begin by examining the null geodesics that govern photon motion in the specified spacetime geometry. The key idea underlying this approach is that the boundary of the shadow is dictated by the set of unstable photon trajectories: photons on these critical orbits either plunge into the BH or escape to infinity, and the transition between these behaviors defines the contour of the observable shadows. By identifying and analyzing these unstable circular photon orbits, we can therefore construct the

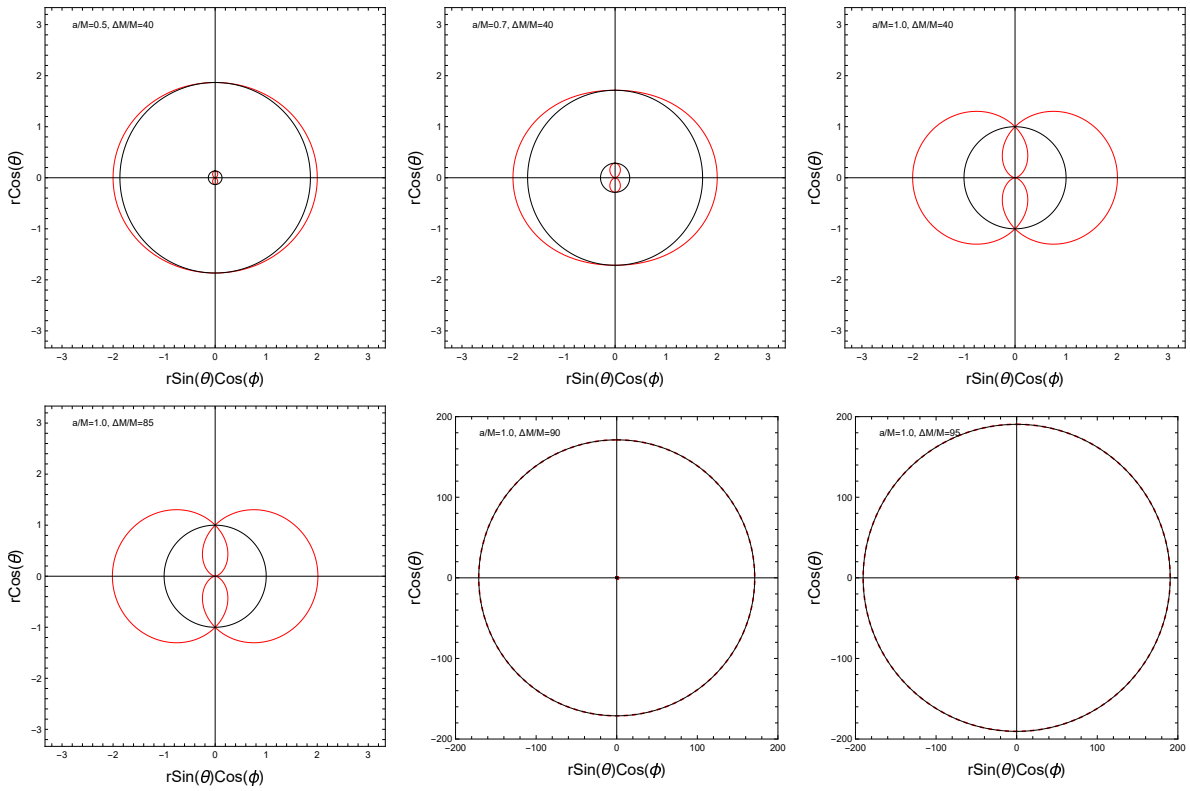

FIG. 4: The first row depicts the ergosphere and horizons for spin parameters $a/M = 0.5, 0.7, 1.0$, while the second row corresponds to DM masses $\Delta M/M = 85, 90, 95$. In each panel, the outermost red curve marks the boundary of the outer ergosphere, and the innermost red curve indicates the boundary of the inner ergosphere. Similarly, the innermost and outermost black curves represent the locations of the inner and outer horizons, respectively.

precise shadow profile associated with the DM surrounded Kerr spacetime.

The equations governing photon trajectories can be derived efficiently through the Hamilton–Jacobi (HJ) formalism. Within this framework, the motion of a test particle is encoded in the HJ equation, which takes the form

$$\frac{\partial S}{\partial \tau} = -\frac{1}{2} g^{\mu\nu} \frac{\partial S}{\partial x^\mu} \frac{\partial S}{\partial x^\nu}, \tag{28}$$

here τ denotes the affine parameter. For the rotating BH under consideration, the metric admits two Killing vector fields, ∂_t and ∂_ϕ, associated respectively with time-translation symmetry and axial symmetry. These geometric symmetries ensure the existence of two conserved quantities along the photon trajectory: the conserved energy E and the conserved

angular momentum L.

$$\begin{aligned} -g_{tt}\dot{t} + g_{t\phi}\dot{\phi} &= -E, \\ g_{t\phi}\dot{t} + g_{\phi\phi}\dot{\phi} &= L. \end{aligned} \tag{29}$$

These two conserved quantities play a central role in the subsequent analysis. Accordingly, we assume that the Jacobi action can be written in the form

$$S = \frac{1}{2}m_0^2\tau - Et + L\phi + S_r(r) + S_\theta(\theta), \tag{30}$$

where m_0 denotes the particle's rest mass. The functions $S_r(r)$ and $S_\theta(\theta)$ depend exclusively on the radial and polar coordinates, respectively, although their explicit forms remain to be determined. Inserting the ansatz for the Jacobi action (30) into the HJ equation (28), and using the fact that photons satisfy the massless condition, the equation separates into the following form

$$\begin{aligned} S_r(r) &= \int^r \frac{\sqrt{\mathcal{R}(r)}}{\Delta(r)}dr, \\ S_\theta(\theta) &= \int^\theta \sqrt{\Theta(\theta)}d\theta, \end{aligned} \tag{31}$$

and

$$\begin{aligned} \mathcal{R}(r) &= \left[E\left(r^2+a^2\right) - aL\right]^2 - \Delta\left(K + (L-aE)^2\right), \\ \Theta(\theta) &= K + \cos^2\theta\left(a^2E^2 - \frac{L^2}{\sin^2\theta}\right), \end{aligned} \tag{32}$$

where K denotes the Carter constant. Because the HJ equation yields one separable relation for each coordinate, the system is completely integrable and therefore admits four independent constants of motion. For photon trajectories, the mass parameter is set to $m_0 = 0$. By differentiating the HJ action with respect to these constants and imposing the condition that the resulting equations vanish, one obtains a set of first-order relations governing null geodesics. Solving this system leads directly to the standard form of the geodesic equations

$$\begin{aligned} \Sigma\frac{dt}{d\tau} &= \frac{r^2+a^2}{\Delta}\left[E\left(r^2+a^2\right) - aL\right] - a\left(aE\sin^2\theta - L\right), \\ \Sigma\frac{dr}{d\tau} &= \sqrt{\mathcal{R}(r)}, \\ \Sigma\frac{d\theta}{d\tau} &= \sqrt{\Theta(\theta)}, \\ \Sigma\frac{d\phi}{d\tau} &= \frac{a}{\Delta}\left[E\left(r^2+a^2\right) - aL\right] - \left(aE - \frac{L}{\sin^2\theta}\right). \end{aligned} \tag{33}$$

The motion of photons in the rotating Kerr BH immersed in DM environment is entirely governed by the geodesic equations given in Eqs. (33). Of particular relevance for shadow

formation are the unstable circular photon orbits, since these trajectories delineate the outermost paths from which light can still escape to a distant observer. The contour of the BH shadow is therefore fixed by the conditions that define such marginally unstable null orbits, namely that the radial potential and its first derivative vanish. In other words, the photon must remain on a circular trajectory while being on the verge of radial instability. These requirements can be succinctly expressed as

$$\mathcal{R}(r)|_{r=r_{\rm ph}} = \left.\frac{d\mathcal{R}(r)}{dr}\right|_{r=r_{\rm ph}} = 0, \quad \left.\frac{d^2\mathcal{R}(r)}{dr^2}\right|_{r=r_{\rm ph}} > 0, \tag{34}$$

where $r_{\rm ph}$ represents the radius of the unstable circular photon orbits. To simplify the analysis, we introduce the dimensionless impact parameters $\xi = L/E$ and $\eta = K/E^2$, which characterize the photon's angular momentum and the Carter constant normalized by its energy. Physically, ξ determines the trajectory's azimuthal bending, while η encodes the motion in the polar direction. By substituting these definitions into Eq. (34) and solving the resulting system, one obtains explicit expressions for ξ and η that describe the critical photon orbits governing the boundary of BH shadow [80, 100–102].

$$\begin{aligned} &\left(r^2 + a^2 - a\xi\right)^2 - \left[\eta + (\xi - a)^2\right]\left(r^2 f(r) + a^2\right) = 0, \\ &4r\left(r^2 + a^2 - a\xi\right) - \left[\eta + (\xi - a)^2\right]\left(2rf(r) + r^2 f'(r)\right) = 0. \end{aligned} \tag{35}$$

At this point, Eq. (35) can be used to solve for

$$\begin{aligned} \xi &= \frac{(r^2 + a^2)\,(rf'(r) + 2f(r)) - 4\,(r^2 f(r) + a^2)}{a\,(rf'(r) + 2f(r))} \\ &= \frac{r\,(a^2 + r^2)\,(m'(r) + 1) + (a^2 - 3r^2)\,m(r)}{a\,(rm'(r) - r + m(r))}, \\ \eta &= \frac{r^3\left(8a^2 f'(r) - r\,(rf'(r) - 2f(r))^2\right)}{a^2\,(rf'(r) + 2f(r))^2} \\ &= \frac{r^3\,(-2rm'(r)\,(2a^2 - 3rm(r) + r^2) + m(r)\,(4a^2 - 9rm(r) + 6r^2) - r^3 m'(r)^2 - r^3)}{a^2\,(rm'(r) - r + m(r))^2}, \end{aligned} \tag{36}$$

here $m(r)$ is mass function defined as in Eq. (3). Note that, in what follows, the radial coordinate r always refers to the photon sphere radius $r_{\rm ph}$. We now proceed, in analogy with the spherically symmetric case, to classify the possible configurations of the photon sphere. Since we set $r_s = r_+$, namely the outer event horizon of the Kerr BH, only the remaining two cases need to be considered.

(1) Case I: $r_s < r_{\rm ph} < r_s + \Delta r_s$. In this regime, we obtain

$$\xi = \frac{\frac{2r\left(a^2+r^2-2r\Lambda(r)\right)}{r(\Lambda'(r)-1)+\Lambda(r)} + a^2 + r^2}{a},$$
$$\eta = \frac{r^3\left(-2r\left(2a^2+r^2-3r\Lambda(r)\right)\Lambda'(r)+\Lambda(r)\left(4a^2+6r^2-9r\Lambda(r)\right)+r^3\left(-\Lambda'(r)^2\right)-r^3\right)}{a^2\left(r\left(\Lambda'(r)-1\right)+\Lambda(r)\right)^2}, \tag{37}$$

with

$$\Lambda(r) = M + \Delta\mathrm{M}\left(3 - \frac{2(r-r_+)}{\Delta r_s}\right)\left(\frac{r-r_+}{\Delta r_s}\right)^2,$$
$$\Lambda'(r) = \frac{6\Delta\mathrm{M}\,(r-r_+)\,(r_+ - r + \Delta \mathrm{r}_s)}{\Delta \mathrm{r}_s^3}. \tag{38}$$

(2) Case II: $r_s + \Delta r_s < r_{\rm ph}$. In this region, we also derive

$$\xi = \frac{a^2(\Delta\mathrm{M}+M+r)+r^2(-3\Delta\mathrm{M}-3M+r)}{a(\Delta\mathrm{M}+M-r)},$$
$$\eta = -\frac{r^3\left(r(-3\Delta\mathrm{M}-3M+r)^2-4a^2(\Delta\mathrm{M}+M)\right)}{a^2(\Delta\mathrm{M}+M-r)^2}. \tag{39}$$

We now proceed to construct the shadow of Kerr BH surrounded by DM. The observer is assumed to be located at (r_o, θ_o), with $r_o \to \infty$ and θ_o representing the angular position on the observer's sky. To characterize the apparent shape of the shadow, we introduce celestial coordinates α and β,

$$\alpha = \lim_{r_o\to\infty}\left(-r_o^2 \sin\theta_o \frac{d\phi}{dr}\right),$$
$$\beta = \lim_{r_o\to\infty}\left(r_o^2 \frac{d\theta}{dr}\right), \tag{40}$$

which correspond to the horizontal and vertical displacements of the photon as seen by the observer. These coordinates are expressed in terms of the conserved impact parameters ξ and η, providing a direct connection between the photon trajectories in BH and the observable shadows profile [80, 82, 100–102]. By employing the null geodesic equations (33), one can express the celestial coordinates in terms of the photon's conserved impact parameters as follows

$$\alpha = -\frac{\xi}{\sin\theta_o},$$
$$\beta = \pm\sqrt{\eta + a^2\cos^2\theta_o - \xi^2\cot^2\theta_o}. \tag{41}$$

For an observer located in the equatorial plane ($\theta_0 = \pi/2$), the expressions for the celestial coordinates simplify considerably, allowing a more straightforward mapping between the

photon's conserved quantities and the apparent shadows outline.

$$\begin{aligned} \alpha &= -\xi, \\ \beta &= \pm\sqrt{\eta}. \end{aligned} \tag{42}$$

This configuration is particularly useful for visualizing the shadows and comparing theoretical predictions with observations. The BH shadows can be constructed by generating a parametric curve in the celestial plane defined by the coordinates α and β, based on Eqs. (41) and (42). The curve is parametrized by the radius of the unstable circular photon orbits, $r_{\rm ph}$. As previously discussed, the shadow corresponds to the region on the observer's sky from which no photons arrive, since light rays within this zone are either captured by the BH or remain on unstable orbits. Consequently, the shape and size of the shadows are entirely determined by these critical photon trajectories.

Figure 5 shows the BH shadows in celestial coordinates for an observer at an inclination angle $\theta_o = 90°$. In the first row, the DM mass is fixed at $\Delta M/M = 40, 60, 80$ to examine the effect of the spin parameter. As the spin increases, the shadow becomes progressively more distorted, with the deformation reaching its maximum in the extremal case, where a distinctive heart-shaped profile emerges.

In the second row, the spin parameter is fixed at $a/M = 0.3, 0.7, 1.0$ to investigate the influence of the DM mass. For relatively small masses, the impact on the shadows remain weak, resulting only in a slight increase in its overall size. However, once the DM mass exceeds a critical value, the shadow undergoes a marked transformation, as shown in the third row. In this regime, the shadow radius becomes significantly larger and grows monotonically with increasing DM mass. These findings indicate that sufficiently large DM masses can strongly modify the BH shadows.

A. Shadow observables

The BH shadow provides a direct imprint of the underlying spacetime geometry, encoding information about both its structure and characteristic length scales. As a result, shadow observations offer a powerful tool for testing gravity in the strong-field regime and for constraining the parameters of BHs. To make quantitative use of this method, one must define observable quantities that capture the size and shape of the shadow. A pioneering framework was introduced by Hioki and Maeda [103, 104], who proposed two key observables to

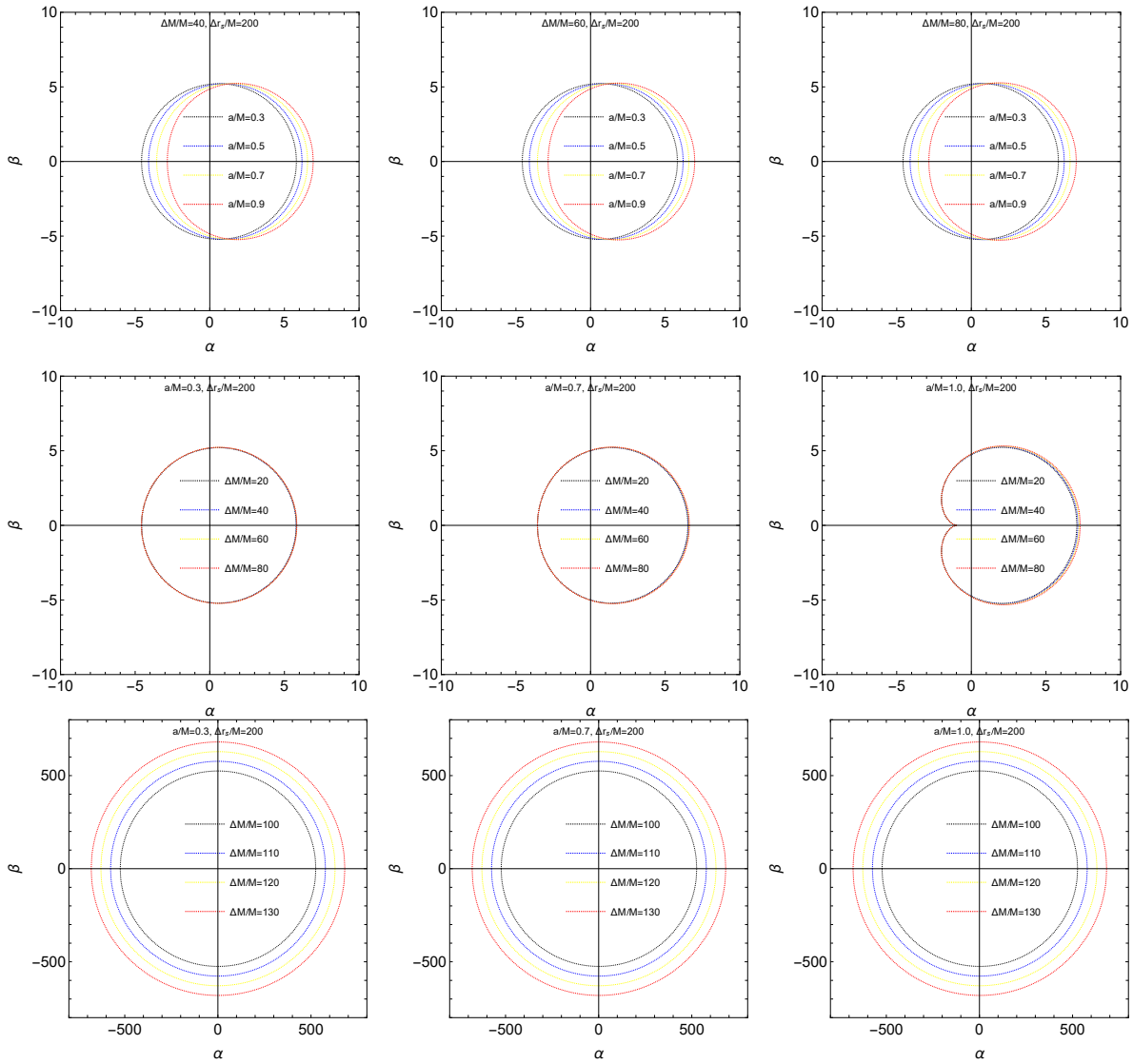

FIG. 5: The figure displays the BH shadows for an observer located at an inclination angle $\theta_o = 90°$. In the first row, the DM mass is held fixed ($\Delta M/M = 40, 60, 80$) to examine the influence of the spin parameter on the shadows. In the second and third rows, the spin parameter is fixed ($a/M = 0.3, 0.7, 1.0$), and the effect of varying the DM mass on the shadows morphology are investigated.

characterize BH shadows. The first is the shadow radius, which measures the overall size of the silhouette. The second is the distortion parameter, designed to quantify departures from circularity. While a perfectly circular shadow is a hallmark of static BHs, rotation generally induces asymmetry and deformation. Accordingly, the distortion parameter provides a convenient means to assess the deviation of rotating BH shadows from the static case, with

the linear shadow radius serving as a practical and directly measurable quantity [103, 105].

As illustrated in Fig. 6, four characteristic points on the shadow boundary are introduced to define its geometry. These include the top point (α_t, β_t) and the bottom point (α_b, β_b), as well as the point $(\alpha_r, 0)$, which corresponds to photons on unstable retrograde circular orbits as seen by an observer in the equatorial plane. Similarly, the point $(\alpha_l, 0)$ is associated with photons following unstable prograde circular orbits. Based on these reference points, the shadow radius can be defined as

$$R_{\rm sh} = \frac{(\alpha_t - \alpha_r)^2 + \beta_t^2}{2(\alpha_r - \alpha_t)}, \tag{43}$$

here we have made use of the shadow's symmetry, which implies $\alpha_b = \alpha_t$ and $\beta_b = -\beta_t$. It is worth noting that when the shadow is perfectly circular, this definition reduces to that of spherically symmetric BH shadows. With these relations in place, we can now proceed to define

$$\delta_s = \frac{(\bar{\alpha}_l - \alpha_l)}{R_{\rm sh}}, \tag{44}$$

where $\bar{\alpha}_l$ represents the horizontal coordinate of the leftmost point of the reference circle. The ratio of the difference between this coordinate and the leftmost point of BH shadow to the shadow radius provides a measure of how much the shadow departs from an ideal circular shape.

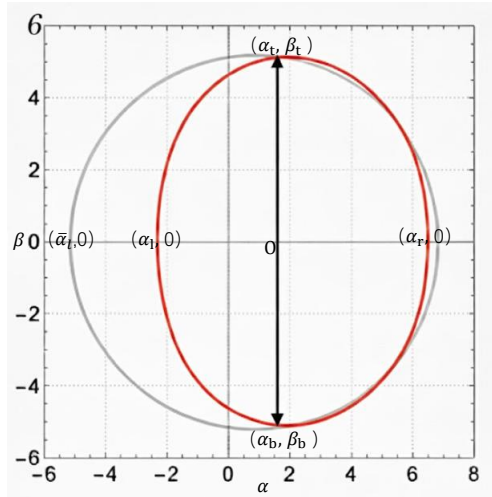

FIG. 6: A schematic illustration of the shadow cast by a rotating BH. In this diagram, the rightmost, leftmost, upper, and lower points on the shadow boundary are denoted by $(\alpha_r, 0)$, $(\alpha_l, 0)$, (α_t, β_t), and (α_b, β_b), respectively, with $\alpha_t = \alpha_b$. In the non-rotating limit, the shadow is symmetric about the vertical axis, and the magnitudes of α_r and α_l become identical.

Figure 7 displays the numerical results for the dependence of the shadow radius and the distortion parameter on the DM mass and the spin. The first row illustrates the variation of the $R_{\rm sh}$ with a and ΔM, while the second row shows the corresponding behavior of the distortion parameter.

From the first column, we observed that for DM masses below the critical value, an increase in the spin parameter leads to a larger shadow radius, and the distortion likewise becomes more pronounced as a approaches the extremal limit. In the second column, where the spin is held fixed, the shadow radius increases approximately linearly with ΔM, whereas the distortion decreases monotonically. This behavior indicates that the presence of DM tends to circularize the shadow.

Once the DM mass exceeds the critical threshold, as shown in the third column, the shadow radius grows by orders of magnitude and the influence of the spin becomes negligible. In this regime, the distortion parameter approaches zero, yielding an almost perfectly circular shadow. This highlights an interesting effect: sufficiently large DM masses can substantially alter the shadow of an axisymmetric BH, effectively restoring circular symmetry.

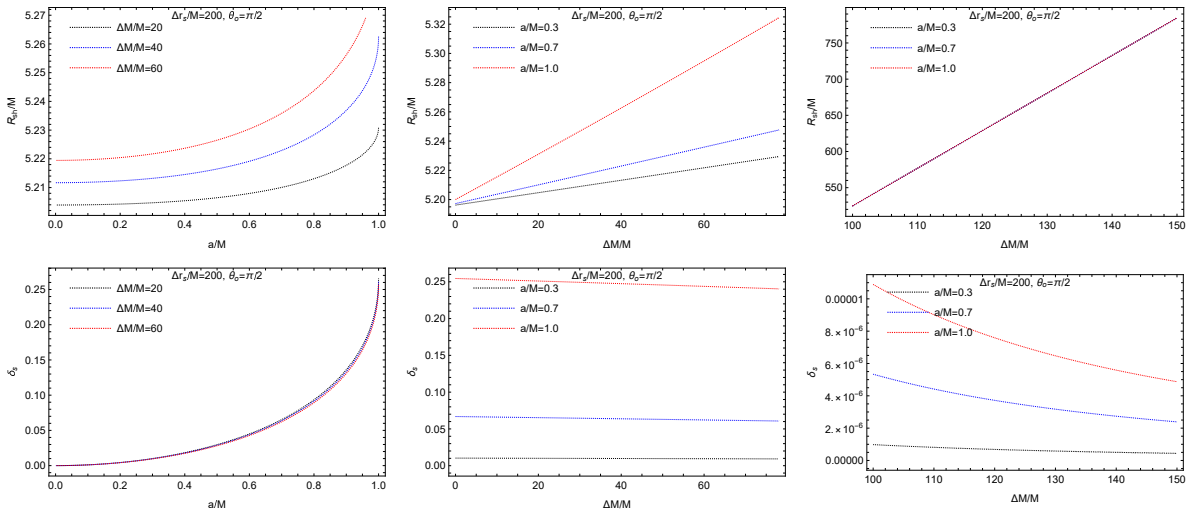

FIG. 7: The first three panels illustrate how the shadow radius varies with the spin parameter and the DM mass, while the last three panels show the dependence of the distortion parameter on these quantities.

B. Energy emission rate

In this section, we investigate the energy emission rate of rotating BH immersed in DM environment. The energy emission rate is a fundamental observable that encodes both the thermodynamic and radiative properties of a BH and is intrinsically determined by the underlying spacetime geometry. In the high-frequency (geometric-optics) regime, the absorption cross section σ_{lim} can be accurately approximated by the area of BH shadow. This correspondence arises because the photon sphere forms a hypersurface of unstable null circular geodesics, which effectively acts as a capture cross section for incident radiation. As a result, from the viewpoint of an observer located at infinity, the BH shadow provides a direct probe of the high-energy absorption cross section. This connection establishes a clear link between the optical appearance of BHs and their radiative behavior [106–113].

For spherically symmetric BHs, the high-energy σ_{lim} which corresponds to the geometrical cross section of the photon sphere [106, 114]. Consequently, this correspondence can be naturally extended to rotating BHs. In Refs. [80, 100, 115], the absorption cross section is defined using $R_{\rm sh}$ ($\sigma_{lim} \approx \pi R_{\rm sh}^2$). however, due to the irregular shape of the shadow, this definition may appear somewhat imprecise. Here, we adopt the average shadow radius to define the cross section, which is expressed as

$$\bar{R} = \frac{1}{2\pi}\int_0^{2\pi}\sqrt{(\alpha-\alpha_c)^2+\beta^2}d\vartheta \tag{45}$$

where $(\alpha_c, 0)$ represents the geometric center of the shadow, and ϑ specifies the angle measured along the shadow boundary from the α axis.

$$\vartheta = \arctan\left(\frac{\beta}{\alpha-\alpha_c}\right). \tag{46}$$

Accordingly, we replace $R_{\rm sh}$ with $barR$, so that the energy emission rate can be written as

$$\frac{d^2E(\omega)}{d\omega dt} = \frac{2\pi^3\omega^3\bar{R}^2}{e^{\omega/T}-1}, \tag{47}$$

here ω denotes the photon frequency, and T is the temperature of BH evaluated at the outer horizon r_+, which is given by [82]

$$\begin{aligned} T &= \lim_{\theta=0, r\to r_+}\frac{\partial_r\sqrt{g_{tt}}}{2\pi\sqrt{g_{rr}}} = \frac{r_+^2 f'(r_+)\left(r_+^2+a^2\right)+2a^2r_+\left(f(r_+)-1\right)}{4\pi\left(r_+^2+a^2\right)^2} \\ &= -\frac{r_+\left(a^2+r_+^2\right)m'(r_+)+(a-r_+)(a+r_+)m(r_+)}{2\pi\left(a^2+r_+^2\right)^2}. \end{aligned} \tag{48}$$

It is evident that, in the limit $m(r)\to M$, the above expression consistently reproduces the Hawking temperature of the Kerr BH.

$$T_{\rm Kerr} = \frac{r_+^2-a^2}{4\pi r_+\left(r_+^2+a^2\right)}. \tag{49}$$

Figure 8 illustrates the variation of energy emission rate as function of the particle frequency in the high-energy regime. For fixed DM mass, the energy emission rate is found to decrease monotonically with increasing spin parameter a. This behavior can be understood from the Hawking temperature given in Eq. (48), which decreases as a grows. As the BH approaches the extremal limit, the corresponding reduction in temperature leads to a pronounced suppression of thermal radiation, and consequently to a weaker energy emission.

When the DM mass remains below the critical value, its influence on the emission rate is marginal, leading at most to a very slight enhancement. Once the DM mass exceeds the critical threshold, however, the Hawking temperature becomes extremely small, and the energy emission rate is strongly suppressed, effectively approaching zero. Such cases are therefore not displayed in the figure. Overall, these results demonstrate that DM can affect

the energy emission properties of rotating BHs, although significant deviations arise only when the DM mass is large enough to induce substantial modifications of the spacetime geometry and its thermodynamic characteristics.

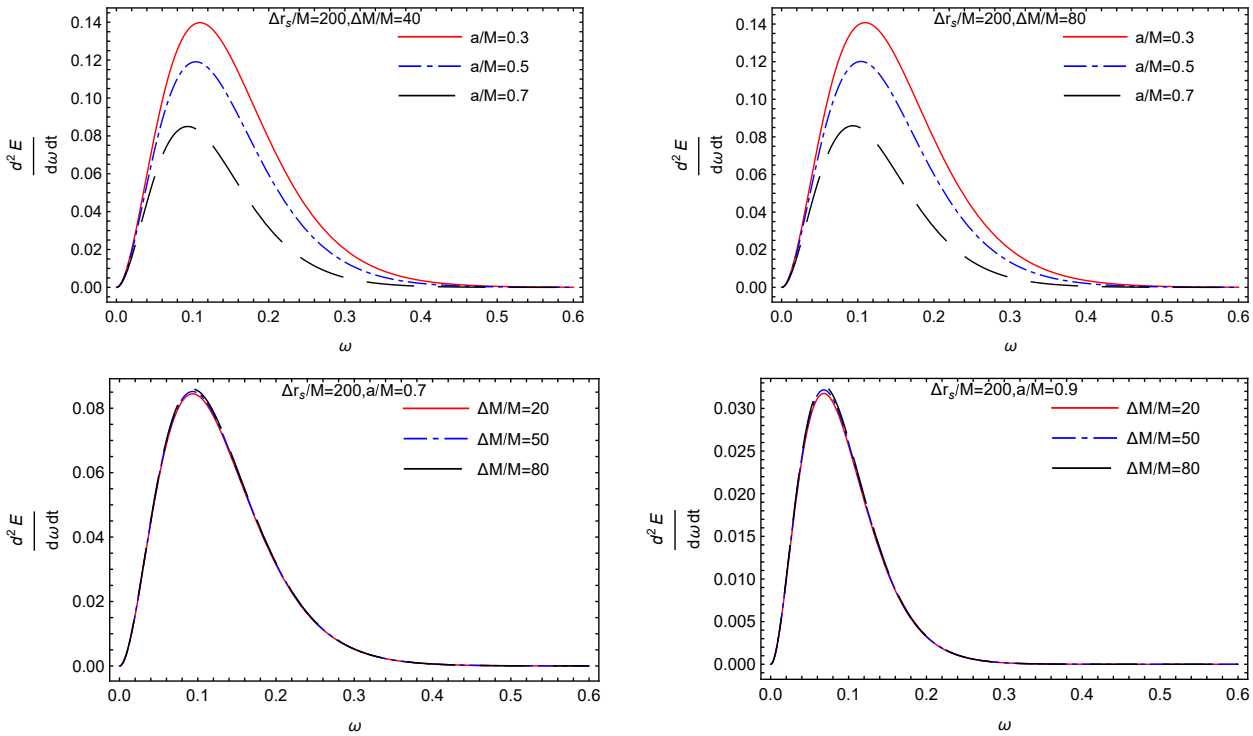

FIG. 8: The energy emission rate as a function of the particle frequency ω for various values of spin a and DM mass ΔM.

V. CONCLUSION

In this work, we have successfully generalized the Schwarzschild BH surrounded by DM to the axisymmetric regime by employing the NJA method. By incorporating piecewise mass function into the Kerr metric, we constructed a rotating BH immersed in DM halo and verified that this solution satisfies the Einstein field equations. Our analysis of the spacetime structure reveals that the presence of DM significantly influences the event horizons and ergospheres. Specifically, when the DM mass exceeds a critical threshold, it induces a substantial expansion of these geometric boundaries, shifting their radial positions by an order of magnitude compared to the vacuum Kerr scenario.

Through the study of null geodesics and the derivation of celestial coordinates, we char-

acterized the morphology of BH shadow and its associated observables. We observed that the shadow radius is positively correlated with the mass of the surrounding DM. As the mass increases, the shadow silhouette grows monotonically. Furthermore, while the spin of BH typically introduces a characteristic asymmetry, the surrounding DM exerts a strong circularizing effect. Consequently, for sufficiently large DM masses, the distortion parameter decreases markedly, causing the shadow to retain a nearly circular shape even in high spin regimes.

Finally, we investigated the energy emission rate based on the high-energy absorption cross section. Our results demonstrate that the emission rate is suppressed by both the BH spin and the presence of the DM halo. Notably, a large DM mass significantly reduces the Hawking temperature, leading to a drastic attenuation of the energy emission rate. Crucially, the substantial structural expansion resulting from high DM mass potentially violates current observational bounds. These results provide strong evidence that the localized DM mass must be constrained below this critical value, or that DM is entirely absent in the BH's immediate vicinity, to maintain consistency with astrophysical measurements.

ACKNOWLEDGMENTS

This study was supported by the National Natural Science Foundation of China (Grant No. 12333008) and the Basic Research Program of Shanxi Province (Grant No. 202503021211204).

Appendix A: Proof that the Einstein Field Equations are satisfied

In this appendix, to prove that the rotating BH (18) incorporating DM, obtained via the NJA, satisfies the Einstein field equations, we first consider the field equations in the following form

$$G_{\mu\nu} = 8\pi T_{\mu\nu}, \tag{A1}$$

where $G_{\mu\nu}$ denotes the Einstein tensor, and $T_{\mu\nu}$ denotes the energy–momentum tensor associated with DM. Through a series of calculations, we write the components of $G_{\mu\nu}$ as

$$
\begin{aligned}
G_{tt} &= \frac{2\mathrm{Y}'\left(a^4\cos^4\theta - a^4\cos^2\theta + a^2r^2 + r^4 - 2\mathrm{Y}r^3\right) - a^2r\sin^2\theta\mathrm{Y}''}{\Sigma^3},\\
G_{rr} &= -\frac{2\mathrm{Y}'r^2}{\Delta\Sigma},\\
G_{\theta\theta} &= -\frac{\mathrm{Y}''a^2r^2\cos^2\theta + 2\mathrm{Y}'a^2\cos^2\theta + \mathrm{Y}''r^3}{\Sigma},\\
G_{t\phi} &= \frac{a\sin^2\theta\left[r\left(a^2+r^2\right)\Sigma\mathrm{Y}'' + 2\mathrm{Y}'\left(\left(a^2+r^2\right)a^2\cos^2\theta - a^2r^2 - r^3(r-2\mathrm{Y})\right)\right]}{\Sigma^3},\\
G_{\phi\phi} &= -\frac{\sin^2\theta\left[r\left(a^2+r^2\right)^2\Sigma\mathrm{Y}'' + 2a^2\mathrm{Y}'\left(\cos^2\theta\left(a^4+3a^2r^2+2r^4-2\mathrm{Y}r^3\right) - a^2r^2 - r^4 + 2\mathrm{Y}r^3\right)\right]}{\Sigma^3}.
\end{aligned}
\tag{A2}
$$

Moreover, we select an energy–momentum tensor constructed from an appropriately selected tetrad of the vector $T^{\mu\nu} = e^\mu_a e^\nu_b T^{ab}$, with its components satisfying $T^{ab} = (\rho, p_r, p_\theta, p_\phi)$. The components of energy–momentum tensor is then expressed in the orthonormal basis as follows

$$
\begin{aligned}
\rho &= \frac{1}{8\pi}e^\mu_t e^\nu_t G_{\mu\nu}, \quad p_r = \frac{1}{8\pi}e^\mu_r e^\nu_r G_{\mu\nu},\\
p_\theta &= \frac{1}{8\pi}e^\mu_\theta e^\nu_\theta G_{\mu\nu}, \quad p_\phi = \frac{1}{8\pi}e^\mu_\phi e^\nu_\phi G_{\mu\nu}.
\end{aligned}
\tag{A3}
$$

Therefore, we need to find a basis that satisfies the field equations. One such orthogonal basis is the following choice

$$
\begin{aligned}
e^\mu_t &= \frac{1}{\sqrt{\Sigma\Delta}}\left(r^2+a^2, 0, 0, a\right),\\
e^\mu_r &= \sqrt{\frac{\Delta}{\Sigma}}(0,1,0,0),\\
e^\mu_\theta &= \frac{1}{\sqrt{\Sigma}}(0,0,1,0),\\
e^\mu_\phi &= -\frac{1}{\sqrt{\Sigma\sin^2\theta}}\left(a\sin^2\theta, 0, 0, 1\right).
\end{aligned}
\tag{A4}
$$

Thus, for the Einstein field equations to be satisfied, the density and pressure of DM under this basis can be derived as

$$
\begin{aligned}
\rho = -p_r &= \frac{\mathrm{m}'(r)r^2}{4\pi\Sigma^2},\\
p_\theta = p_\phi &= p_r - \frac{\mathrm{m}''(r)r + 2\mathrm{m}'(r)}{8\pi\Sigma},
\end{aligned}
\tag{A5}
$$

where, $m'(r)$ denotes $dm(r)/dr$. These results indicate that (23) is indeed a solution to Einstein field equations.

---

[1] Kazunori Akiyama et al. First Sagittarius A* Event Horizon Telescope Results. I. The Shadow of the Supermassive Black Hole in the Center of the Milky Way. *Astrophys. J. Lett.*, 930(2):L12, 2022.

[2] Kazunori Akiyama et al. First Sagittarius A* Event Horizon Telescope Results. VI. Testing the Black Hole Metric. *Astrophys. J. Lett.*, 930(2):L17, 2022.

[3] Kazunori Akiyama et al. First M87 Event Horizon Telescope Results. I. The Shadow of the Supermassive Black Hole. *Astrophys. J. Lett.*, 875:L1, 2019.

[4] Kazunori Akiyama et al. First M87 Event Horizon Telescope Results. IV. Imaging the Central Supermassive Black Hole. *Astrophys. J. Lett.*, 875(1):L4, 2019.

[5] Kazunori Akiyama et al. First M87 Event Horizon Telescope Results. V. Physical Origin of the Asymmetric Ring. *Astrophys. J. Lett.*, 875(1):L5, 2019.

[6] Kazunori Akiyama et al. First M87 Event Horizon Telescope Results. III. Data Processing and Calibration. *Astrophys. J. Lett.*, 875(1):L3, 2019.

[7] Kazunori Akiyama et al. First M87 Event Horizon Telescope Results. VI. The Shadow and Mass of the Central Black Hole. *Astrophys. J. Lett.*, 875(1):L6, 2019.

[8] Kazunori Akiyama et al. First Sagittarius A* Event Horizon Telescope Results. II. EHT and Multiwavelength Observations, Data Processing, and Calibration. *Astrophys. J. Lett.*, 930(2):L13, 2022.

[9] Kazunori Akiyama et al. First Sagittarius A* Event Horizon Telescope Results. III. Imaging of the Galactic Center Supermassive Black Hole. *Astrophys. J. Lett.*, 930(2):L14, 2022.

[10] Kazunori Akiyama et al. First Sagittarius A* Event Horizon Telescope Results. IV. Variability, Morphology, and Black Hole Mass. *Astrophys. J. Lett.*, 930(2):L15, 2022.

[11] Kazunori Akiyama et al. First Sagittarius A* Event Horizon Telescope Results. V. Testing Astrophysical Models of the Galactic Center Black Hole. *Astrophys. J. Lett.*, 930(2):L16, 2022.

[12] Nicholas S. Conroy, Michi Bauböck, Vedant Dhruv, Daeyoung Lee, Avery E. Broderick, Chi-kwan Chan, Boris Georgiev, Abhishek V. Joshi, Ben Prather, and Charles F. Gammie.

Rotation in Event Horizon Telescope Movies. *Astrophys. J.*, 951(1):46, 2023.

[13] R. Abuter et al. Polarimetry and astrometry of NIR flares as event horizon scale, dynamical probes for the mass of Sgr A*. *Astron. Astrophys.*, 677:L10, 2023.

[14] Michael D. Johnson et al. Universal interferometric signatures of a black hole's photon ring. *Sci. Adv.*, 6(12):eaaz1310, 2020.

[15] Roman Gold et al. Verification of Radiative Transfer Schemes for the EHT. *Astrophys. J.*, 897(2):148, 2020.

[16] Pawel O. Mazur. Black hole uniqueness theorems. 12 2000.

[17] Clifford M. Will. The Confrontation between General Relativity and Experiment. *Living Rev. Rel.*, 17:4, 2014.

[18] Kent Yagi and Leo C. Stein. Black Hole Based Tests of General Relativity. *Class. Quant. Grav.*, 33(5):054001, 2016.

[19] Roger Penrose. Gravitational collapse and space-time singularities. *Phys. Rev. Lett.*, 14:57–59, 1965.

[20] Roy P. Kerr. Gravitational field of a spinning mass as an example of algebraically special metrics. *Phys. Rev. Lett.*, 11:237–238, 1963.

[21] S. Chandrasekhar. *The mathematical theory of black holes.* 1983.

[22] J. L. Synge. The Escape of Photons from Gravitationally Intense Stars. *Mon. Not. Roy. Astron. Soc.*, 131(3):463–466, 1966.

[23] J. P. Luminet. Image of a spherical black hole with thin accretion disk. *Astron. Astrophys.*, 75:228–235, 1979.

[24] J. M. Bardeen, B. Carter, and S. W. Hawking. The four laws of black hole mechanics. *Communications in Mathematical Physics*, 31(2):161–170, June 1973.

[25] Peng-Cheng Li, Minyong Guo, and Bin Chen. Shadow of a Spinning Black Hole in an Expanding Universe. *Phys. Rev. D*, 101(8):084041, 2020.

[26] Haopeng Yan. Influence of a plasma on the observational signature of a high-spin Kerr black hole. *Phys. Rev. D*, 99(8):084050, 2019.

[27] Robie A. Hennigar, Mohammad Bagher Jahani Poshteh, and Robert B. Mann. Shadows, Signals, and Stability in Einsteinian Cubic Gravity. *Phys. Rev. D*, 97(6):064041, 2018.

[28] R. A. Konoplya. Shadow of a black hole surrounded by dark matter. *Phys. Lett. B*, 795:1–6, 2019.

[29] Cosimo Bambi and Katherine Freese. Apparent shape of super-spinning black holes. *Phys. Rev. D*, 79:043002, 2009.

[30] Roman A. Konoplya, Thomas Pappas, and Alexander Zhidenko. Einstein-scalar–Gauss-Bonnet black holes: Analytical approximation for the metric and applications to calculations of shadows. *Phys. Rev. D*, 101(4):044054, 2020.

[31] Shao-Wen Wei, Yuan-Chuan Zou, Yu-Xiao Liu, and Robert B. Mann. Curvature radius and Kerr black hole shadow. *JCAP*, 08:030, 2019.

[32] Shao-Wen Wei, Yu-Xiao Liu, and Robert B. Mann. Intrinsic curvature and topology of shadows in Kerr spacetime. *Phys. Rev. D*, 99(4):041303, 2019.

[33] Hui-Min Wang, Yu-Meng Xu, and Shao-Wen Wei. Shadows of Kerr-like black holes in a modified gravity theory. *JCAP*, 03:046, 2019.

[34] Cheng Liu, Tao Zhu, Qiang Wu, Kimet Jusufi, Mubasher Jamil, Mustapha Azreg-Aïnou, and Anzhong Wang. Shadow and quasinormal modes of a rotating loop quantum black hole. *Phys. Rev. D*, 101(8):084001, 2020. [Erratum: Phys.Rev.D 103, 089902 (2021)].

[35] Rahul Kumar, Sushant G. Ghosh, and Anzhong Wang. Shadow cast and deflection of light by charged rotating regular black holes. *Phys. Rev. D*, 100(12):124024, 2019.

[36] Takayuki Ohgami and Nobuyuki Sakai. Wormhole shadows. *Phys. Rev. D*, 91(12):124020, 2015.

[37] Petya G. Nedkova, Vassil K. Tinchev, and Stoytcho S. Yazadjiev. Shadow of a rotating traversable wormhole. *Phys. Rev. D*, 88(12):124019, 2013.

[38] Rajibul Shaikh. Shadows of rotating wormholes. *Phys. Rev. D*, 98(2):024044, 2018.

[39] Muhammed Amir, Ayan Banerjee, and Sunil D. Maharaj. Shadow of charged wormholes in Einstein–Maxwell–dilaton theory. *Annals Phys.*, 400:198–207, 2019.

[40] Muhammed Amir, Kimet Jusufi, Ayan Banerjee, and Sudan Hansraj. Shadow images of Kerr-like wormholes. *Class. Quant. Grav.*, 36(21):215007, 2019.

[41] Xiaobao Wang, Peng-Cheng Li, Cheng-Yong Zhang, and Minyong Guo. Novel shadows from the asymmetric thin-shell wormhole. *Phys. Lett. B*, 811:135930, 2020.

[42] Zhe Chang and Qing-Hua Zhu. Does the shape of the shadow of a black hole depend on motional status of an observer? *Phys. Rev. D*, 102(4):044012, 2020.

[43] Samuel E. Gralla and Alexandru Lupsasca. Observable shape of black hole photon rings. *Phys. Rev. D*, 102(12):124003, 2020.

[44] N. Jarosik et al. Seven-Year Wilkinson Microwave Anisotropy Probe (WMAP) Observations: Sky Maps, Systematic Errors, and Basic Results. *Astrophys. J. Suppl.*, 192:14, 2011.

[45] Prajwal Raj Kafle, Sanjib Sharma, Geraint F. Lewis, and Joss Bland-Hawthorn. On the Shoulders of Giants: Properties of the Stellar Halo and the Milky Way Mass Distribution. *Astrophys. J.*, 794(1):59, 2014.

[46] Giuseppina Battaglia, Amina Helmi, Heather Morrison, Paul Harding, Edward W. Olszewski, Mario Mateo, Kenneth C. Freeman, John Norris, and Stephen A. Shectman. The Radial velocity dispersion profile of the Galactic Halo: Constraining the density profile of the dark halo of the Milky Way. *Mon. Not. Roy. Astron. Soc.*, 364:433–442, 2005. [Erratum: Mon.Not.Roy.Astron.Soc. 370, 1055 (2006)].

[47] R. Bernabei et al. First model independent results from DAMA/LIBRA-phase2. *Nucl. Phys. Atom. Energy*, 19(4):307–325, 2018.

[48] C. Amole et al. Dark Matter Search Results from the PICO-60 C_3F_8 Bubble Chamber. *Phys. Rev. Lett.*, 118(25):251301, 2017.

[49] G. Angloher et al. Results on light dark matter particles with a low-threshold CRESST-II detector. *Eur. Phys. J. C*, 76(1):25, 2016.

[50] R. Bernabei et al. Final model independent result of DAMA/LIBRA-phase1. *Eur. Phys. J. C*, 73:2648, 2013.

[51] R. Bernabei et al. First results from DAMA/LIBRA and the combined results with DAMA/NaI. *Eur. Phys. J. C*, 56:333–355, 2008.

[52] Naoki Tsukamoto. Black hole shadow in an asymptotically-flat, stationary, and axisymmetric spacetime: The Kerr-Newman and rotating regular black holes. *Phys. Rev. D*, 97(6):064021, 2018.

[53] Kei-ichi Maeda, Vitor Cardoso, and Anzhong Wang. Einstein cluster as central spiky distribution of galactic dark matter. *Phys. Rev. D*, 111(4):044060, 2025.

[54] Zibo Shen, Anzhong Wang, and Shaoyu Yin. Inner radius and energy conditions of dark matter halos surrounding Schwarzschild black holes. *Phys. Lett. B*, 862:139300, 2025.

[55] Chen-Kai Qiao and Ping Su. Time delay of light in the gravitational lensing of supermassive black holes in dark matter halos. *Eur. Phys. J. C*, 84(10):1032, 2024.

[56] S. R. Wu, B. Q. Wang, Z. W. Long, and Hao Chen. Rotating black holes surrounded by a dark matter halo in the galactic center of M87 and Sgr A$*$. *Phys. Dark Univ.*, 44:101455,

2024.

[57] Salvatore Capozziello, Soroush Zare, Luis M. Nieto, and Hassan Hassanabadi. Modified Kerr black holes surrounded by dark matter spike. *Phys. Dark Univ.*, 50:102065, 2025.

[58] S. Capozziello, S. Zare, D. F. Mota, and H. Hassanabadi. Dark matter spike around Bumblebee black holes. 3 2023.

[59] Zhaoyi Xu, Xiaobo Gong, and Shuang-Nan Zhang. Black hole immersed dark matter halo. *Phys. Rev. D*, 101(2):024029, 2020.

[60] Kimet Jusufi, Mubasher Jamil, and Tao Zhu. Shadows of Sgr A* black hole surrounded by superfluid dark matter halo. *Eur. Phys. J. C*, 80(5):354, 2020.

[61] Sumarna Haroon, Mubasher Jamil, Kimet Jusufi, Kai Lin, and Robert B. Mann. Shadow and Deflection Angle of Rotating Black Holes in Perfect Fluid Dark Matter with a Cosmological Constant. *Phys. Rev. D*, 99(4):044015, 2019.

[62] Reggie C. Pantig. Apparent and emergent dark matter around a Schwarzschild black hole. *Phys. Dark Univ.*, 45:101550, 2024.

[63] Sumanta Chakraborty, Geoffrey Compère, and Ludovico Machet. Tidal Love numbers and quasinormal modes of the Schwarzschild-Hernquist black hole. *Phys. Rev. D*, 112(2):024015, 2025.

[64] Justin C. Feng, Sumanta Chakraborty, and Vitor Cardoso. Shielding a charged black hole. *Phys. Rev. D*, 107(4):044050, 2023.

[65] Shauvik Biswas, Chiranjeeb Singha, and Sumanta Chakraborty. Galactic wormholes: Geometry, stability, and echoes. *Phys. Rev. D*, 109(6):064043, 2024.

[66] Ali Övgün and Reggie C. Pantig. Black hole in the Dekel-Zhao dark matter profile. *Phys. Lett. B*, 864:139398, 2025.

[67] Mohan Khatri and Pradyumn Kumar Sahoo. Existence of wormhole in Dekel–Zhao dark matter halo. *Phys. Dark Univ.*, 49:102042, 2025.

[68] A. Errehymy. Null geodesics and shadows of Dekel-Zhao-type dark matter black holes with a quintessential field: Constraints from EHT observations of M87* and Sgr A*. *Phys. Lett. B*, 870:139945, 2025.

[69] R. A. Konoplya. Shadow of a black hole surrounded by dark matter. *Phys. Lett. B*, 795:1–6, 2019.

[70] Sohan Kumar Jha. Shadow, ISCO, quasinormal modes, Hawking spectrum, weak gravi-

tational lensing, and parameter estimation of a Schwarzschild black hole surrounded by a Dehnen type dark matter halo. *JCAP*, 03:054, 2025.

[71] Zdeněk Stuchlík and Jaroslav Vrba. Geodesic Model of HF QPOs Tested for Black Holes in Spacetimes Reflecting the Effect of Surrounding Dark Matter. *Astrophys. J.*, 935(2):91, August 2022.

[72] Che-Yu Chen, Chiang-Mei Chen, and Nobuyoshi Ohta. Shadow of rotating black holes with consistent thermodynamics. *Phys. Rev. D*, 113(4):044044, 2026.

[73] Qian Wan, Yehui Hou, and Minyong Guo. Probing the scalar hair of rotating Horndeski black holes through thick disk images. *Phys. Rev. D*, 113(8):083023, 2026.

[74] Naoki Tsukamoto, Zilong Li, and Cosimo Bambi. Constraining the spin and the deformation parameters from the black hole shadow. *JCAP*, 06:043, 2014.

[75] Sourabh Nampalliwar, Saurabh Kumar, Kimet Jusufi, Qiang Wu, Mubasher Jamil, and Paolo Salucci. Modeling the Sgr A* Black Hole Immersed in a Dark Matter Spike. *Astrophys. J.*, 916(2):116, 2021.

[76] Ben Moore, Thomas R. Quinn, Fabio Governato, Joachim Stadel, and George Lake. Cold collapse and the core catastrophe. *Mon. Not. Roy. Astron. Soc.*, 310:1147–1152, 1999.

[77] Julio F. Navarro, Carlos S. Frenk, and Simon D. M. White. Simulations of x-ray clusters. *Mon. Not. Roy. Astron. Soc.*, 275:720–740, 1995.

[78] Yasushi Suto, Shin Sasaki, and Nobuyoshi Makino. Gas density and x-ray surface brightness profiles of clusters of galaxies from dark matter halo potentials: Beyond the isothermal Beta model. *Astrophys. J.*, 509:544–550, 1998.

[79] Chiara Di Paolo, Fabrizio Nesti, and Francesco L. Villante. Phase space mass bound for fermionic dark matter from dwarf spheroidal galaxies. *Mon. Not. Roy. Astron. Soc.*, 475(4):5385–5397, 2018.

[80] Xian Hou, Zhaoyi Xu, and Jiancheng Wang. Rotating Black Hole Shadow in Perfect Fluid Dark Matter. *JCAP*, 12:040, 2018.

[81] Xian Hou, Zhaoyi Xu, Ming Zhou, and Jiancheng Wang. Black hole shadow of Sgr A* in dark matter halo. *JCAP*, 07:015, 2018.

[82] Sumarna Haroon, Mubasher Jamil, Kimet Jusufi, Kai Lin, and Robert B. Mann. Shadow and Deflection Angle of Rotating Black Holes in Perfect Fluid Dark Matter with a Cosmological Constant. *Phys. Rev. D*, 99(4):044015, 2019.

[83] Pedro V. P. Cunha, Carlos A. R. Herdeiro, Eugen Radu, and Helgi F. Runarsson. Shadows of Kerr black holes with scalar hair. *Phys. Rev. Lett.*, 115(21):211102, 2015.

[84] Ahmadjon Abdujabbarov, Bobir Toshmatov, Zdeněk Stuchlík, and Bobomurat Ahmedov. Shadow of the rotating black hole with quintessential energy in the presence of plasma. *Int. J. Mod. Phys. D*, 26(06):1750051, 2016.

[85] K. Saurabh and Kimet Jusufi. Imprints of dark matter on black hole shadows using spherical accretions. *Eur. Phys. J. C*, 81(6):490, 2021.

[86] Reggie C. Pantig, Paul K. Yu, Emmanuel T. Rodulfo, and Ali Övgün. Shadow and weak deflection angle of extended uncertainty principle black hole surrounded with dark matter. *Annals Phys.*, 436:168722, 2022.

[87] Reggie C. Pantig and Emmanuel T. Rodulfo. Weak deflection angle of a dirty black hole. *Chin. J. Phys.*, 66:691–702, 2020.

[88] Akhil Uniyal, Reggie C. Pantig, and Ali Övgün. Probing a non-linear electrodynamics black hole with thin accretion disk, shadow, and deflection angle with M87* and Sgr A* from EHT. *Phys. Dark Univ.*, 40:101178, 2023.

[89] Volker Perlick and Oleg Yu. Tsupko. Calculating black hole shadows: Review of analytical studies. *Phys. Rept.*, 947:1–39, 2022.

[90] Volker Perlick, Oleg Yu. Tsupko, and Gennady S. Bisnovatyi-Kogan. Influence of a plasma on the shadow of a spherically symmetric black hole. *Phys. Rev. D*, 92(10):104031, 2015.

[91] E. T. Newman and A. I. Janis. Note on the Kerr spinning particle metric. *J. Math. Phys.*, 6:915–917, 1965.

[92] E T. Newman, E. Couch, K. Chinnapared, A. Exton, A. Prakash, and R. Torrence. Metric of a Rotating, Charged Mass. *J. Math. Phys.*, 6:918–919, 1965.

[93] Mustapha Azreg-Aïnou. Generating rotating regular black hole solutions without complexification. *Phys. Rev. D*, 90(6):064041, 2014.

[94] Mustapha Azreg-Aïnou. From static to rotating to conformal static solutions: Rotating imperfect fluid wormholes with(out) electric or magnetic field. *Eur. Phys. J. C*, 74(5):2865, 2014.

[95] Rahul Kumar Walia, Sunil D. Maharaj, and Sushant G. Ghosh. Rotating Black Holes in Horndeski Gravity: Thermodynamic and Gravitational Lensing. *Eur. Phys. J. C*, 82:547, 2022.

[96] Kimet Jusufi, Mubasher Jamil, Paolo Salucci, Tao Zhu, and Sumarna Haroon. Black Hole Surrounded by a Dark Matter Halo in the M87 Galactic Center and its Identification with Shadow Images. *Phys. Rev. D*, 100(4):044012, 2019.

[97] He-Xu Zhang, Yuan Chen, Tian-Chi Ma, Peng-Zhang He, and Jian-Bo Deng. Bardeen black hole surrounded by perfect fluid dark matter. *Chin. Phys. C*, 45(5):055103, 2021.

[98] Mustapha Azreg-Aïnou. From static to rotating to conformal static solutions: Rotating imperfect fluid wormholes with(out) electric or magnetic field. *Eur. Phys. J. C*, 74(5):2865, 2014.

[99] Mustapha Azreg-Aïnou. Generating rotating regular black hole solutions without complexification. *Phys. Rev. D*, 90(6):064041, 2014.

[100] Kimet Jusufi, Mubasher Jamil, Paolo Salucci, Tao Zhu, and Sumarna Haroon. Black Hole Surrounded by a Dark Matter Halo in the M87 Galactic Center and its Identification with Shadow Images. *Phys. Rev. D*, 100(4):044012, 2019.

[101] Odil Yunusov, Javlon Rayimbaev, Furkat Sarikulov, Muhammad Zahid, Ahmadjon Abdujabbarov, and Zdeněk Stuchlík. Rotating charged black holes in EMS theory: shadow studies and constraints from EHT observations. *Eur. Phys. J. C*, 84(12):1240, 2024.

[102] Uma Papnoi and Farruh Atamurotov. Rotating charged black hole in 4D Einstein–Gauss–Bonnet gravity: Photon motion and its shadow. *Phys. Dark Univ.*, 35:100916, 2022.

[103] Kenta Hioki and Kei-ichi Maeda. Measurement of the Kerr Spin Parameter by Observation of a Compact Object's Shadow. *Phys. Rev. D*, 80:024042, 2009.

[104] Jan Schee and Zdenek Stuchlik. Optical phenomena in the field of braneworld Kerr black holes. *Int. J. Mod. Phys. D*, 18:983–1024, 2009.

[105] Muhammed Amir and Sushant G. Ghosh. Shapes of rotating nonsingular black hole shadows. *Phys. Rev. D*, 94(2):024054, 2016.

[106] Bahram Mashhoon. Scattering of Electromagnetic Radiation from a Black Hole. *Phys. Rev. D*, 7:2807–2814, 1973.

[107] R. Fabbri. Scattering and absorption of electromagnetic waves by a Schwarzschild black hole. *Phys. Rev. D*, 12:933–942, 1975.

[108] Don N. Page. Particle Emission Rates from a Black Hole: Massless Particles from an Uncharged, Nonrotating Hole. *Phys. Rev. D*, 13:198–206, 1976.

[109] W. G. Unruh. Absorption Cross-Section of Small Black Holes. *Phys. Rev. D*, 14:3251–3259,

1976.

[110] Sumit R. Das, Gary W. Gibbons, and Samir D. Mathur. Universality of low-energy absorption cross-sections for black holes. *Phys. Rev. Lett.*, 78:417–419, 1997.

[111] Eylee Jung and D. K. Park. Effect of scalar mass in the absorption and emission spectra of Schwarzschild black hole. *Class. Quant. Grav.*, 21:3717–3732, 2004.

[112] Chris Doran, Anthony Lasenby, Sam Dolan, and Ian Hinder. Fermion absorption cross section of a Schwarzschild black hole. *Phys. Rev. D*, 71:124020, 2005.

[113] Luis C. B. Crispino, Ednilton S. Oliveira, Atsushi Higuchi, and George E. A. Matsas. Absorption cross section of electromagnetic waves for Schwarzschild black holes. *Phys. Rev. D*, 75:104012, 2007.

[114] Yves Decanini, Gilles Esposito-Farese, and Antoine Folacci. Universality of high-energy absorption cross sections for black holes. *Phys. Rev. D*, 83:044032, 2011.

[115] Shao-Wen Wei and Yu-Xiao Liu. Observing the shadow of Einstein-Maxwell-Dilaton-Axion black hole. *JCAP*, 11:063, 2013.